
SPATIAL-AND-FREQUENCY-AWARE RESTORATION METHOD FOR IMAGES BASED ON DIFFUSION MODELS

Kyung Sung Lee*
kslee0304@snu.ac.kr

Donggyu Lee*
dglee442@snu.ac.kr

Myungjoo Kang*
mkang@snu.ac.kr

ABSTRACT

Diffusion models have recently emerged as a promising framework for Image Restoration (IR), owing to their ability to produce high-quality reconstructions and their compatibility with established methods. Existing methods for solving noisy inverse problems in IR, considers the pixel-wise data-fidelity. In this paper, we propose SaFaRI, a spatial-and-frequency-aware diffusion model for IR with Gaussian noise. Our model encourages images to preserve data-fidelity in both the spatial and frequency domains, resulting in enhanced reconstruction quality. We comprehensively evaluate the performance of our model on a variety of noisy inverse problems, including inpainting, denoising, and super-resolution. Our thorough evaluation demonstrates that SaFaRI achieves state-of-the-art performance on both the ImageNet datasets and FFHQ datasets, outperforming existing zero-shot IR methods in terms of LPIPS and FID metrics.

1 Introduction

In the field of Image Restoration (IR), the overarching objective is to reconstruct an original image from a degraded or corrupted version of it. A classic approach Rudin et al. [1992] is to use a variational model, which minimizes a cost function that includes a data-fidelity term and a regularization term Benning and Burger [2018]. The data-fidelity term measures the difference between the restored image and the ground truth image, while the regularization term encourages the restored image to be smooth or have other desirable properties. If the measurement noise is Gaussian, the data-fidelity term is

$$\|\mathbf{y} - \mathbf{Ax}\|_2^2, \quad (1)$$

where \mathbf{y} is a measurement, \mathbf{A} is a degradation operator and \mathbf{x} is a reconstructed image.

Meanwhile, diffusion models have gained widespread recognition as foundational models for generative modeling, offering a robust and flexible approach to data generation Ho et al. [2020], Song et al. [2021], Dhariwal and Nichol [2021a].

It exhibits remarkable capabilities in diverse image restoration tasks, encompassing deblurring, super-resolution, inpainting, and JPEG artifact removal. Notably, it achieves this through a zero-shot learning approach, effectively utilizing the generative priors embedded within a pre-trained model. Choi et al. [2021], Kwar et al. [2021, 2022a], Wang et al. [2022], Chung et al. [2023], Zhu et al. [2023], Chung et al. [2022a,b], Song et al. [2022], Lugmayr et al. [2022], Fei et al. [2023], Kwar et al. [2022b]. Numerous image restoration approaches employ conditional sampling to generate the desired restored image. This involves starting with pure noise and gradually denoising the image using diffusion models while concurrently pushing the data in the direction that minimizes data fidelity Chung et al. [2023], Song et al. [2022], Chung et al. [2022b], hence minimizing (1).

In this work, our primary objective extends beyond mere pixel-level data-fidelity to encompass perceptual data-fidelity. There have been numerous studies Chen and Ford [1994], Jam et al. [2021], Lukac [2017], Wang et al. [2018] on image restoration that consider perceptual information. In IR, the improvement of perceptual information is essential for images, and hence, for performance Yang et al. [2020], Ma et al. [2022], Li et al. [2016]. Convolution operator and Fourier transform are two representative operators that handle perceptual information in images Yang et al. [2023],

*Department of Mathematical Sciences, Seoul National University, Seoul, South Korea

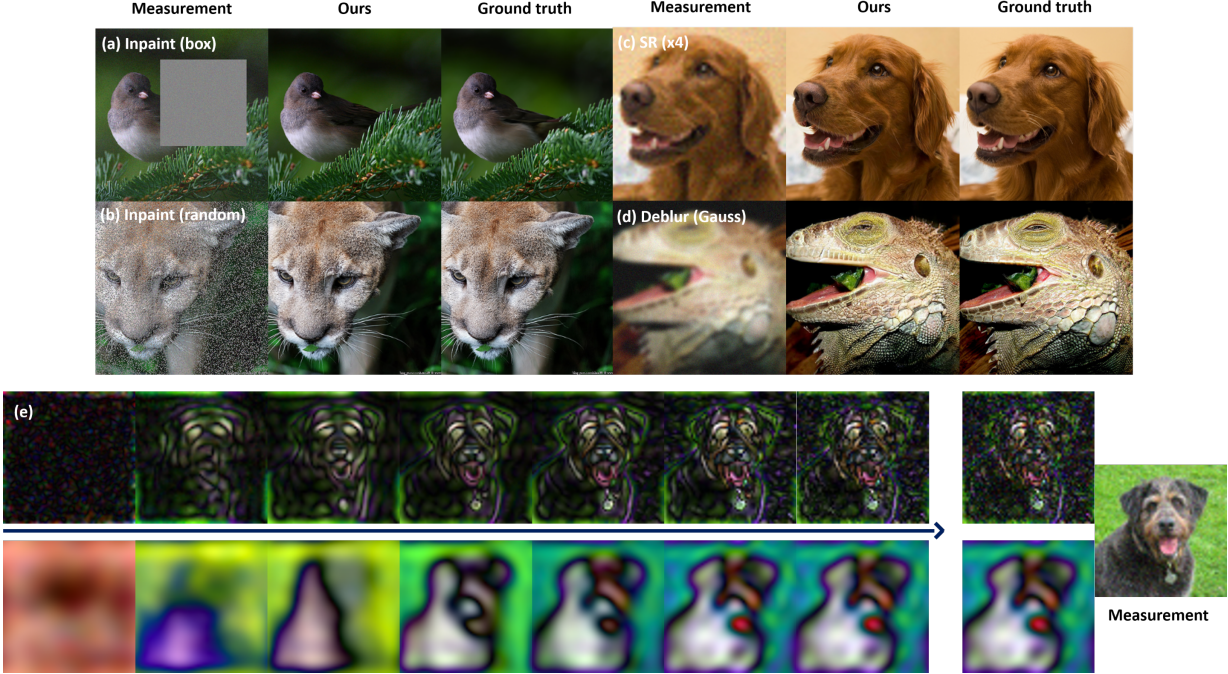


Figure 1: Examples and visual explanations of our method’s functionality. (a)-(d): Results of the image restoration tasks: box-type inpainting, random-type inpainting, Gaussian deblurring and super resolution, respectively. (e): The first row illustrates the sequential changes in $A\hat{x}_{0|t}$ after applying high-pass filtering, leading to the final filtered image of \mathbf{y} , while the second row presents the low-pass counterparts.

Yuan et al. [2023], Sheng et al. [2022], Fuoli et al. [2021]. These two operators are associated with spatial and frequency perceptual features, respectively Ayyoubzadeh and Wu [2021], Shao et al. [2023].

Drawing inspiration from these observations propose SaFaRI, a spatial-and-frequency-aware restoration method for images using diffusion model. SaFaRI is constructed by refining pixel-wise data fidelity using upsampling and Fourier Transform to enhance perceptual quality. Spatial-frequency-aware priors are integrated into the diffusion process in SaFaRI, allowing it to capture both low-level and high-level image features during restoration. We show that our method achieves significantly better performance than other zero-shot diffusion model-based image restoration methods.

2 Background

2.1 Score-based Diffusion Models

The diffusion process represents the corruption of a clean data point by adding noise. This process is mathematically represented using SDE Song et al. [2021], which captures the dynamic evolution of the data point as noise is gradually injected. The SDE governing the forward diffusion process is given by:

$$d\mathbf{x} = \mathbf{f}(\mathbf{x}, t)dt + g(t)d\mathbf{w}, \quad (2)$$

where $\mathbf{f} : \mathbb{R}^d \times [0, 1] \rightarrow \mathbb{R}^d$ and $g : [0, 1] \rightarrow \mathbb{R}$ are drift and diffusion coefficient respectively and \mathbf{w} is the standard Wiener process.

The associated reverse SDE Anderson [1982] is expressed as:

$$d\mathbf{x} = [\mathbf{f}(\mathbf{x}, t) - g^2(t)\nabla_{\mathbf{x}} \log p(\mathbf{x})] dt + g(t)d\bar{\mathbf{w}}. \quad (3)$$

Here, dt is an infinitesimal negative time step and $\bar{\mathbf{w}}$ is the standard Wiener process running backward in time. The score function $\nabla_{\mathbf{x}} \log p_t(\mathbf{x})$ can be approximated by a neural network $\mathbf{s}_\theta(\mathbf{x}, t)$ with score-matching Song and Ermon [2019], Song et al. [2021] objective:

$$\mathbb{E}_t \left[\lambda_t \mathbb{E}_{\mathbf{x}(0)} \mathbb{E}_{\mathbf{x}(t)|\mathbf{x}(0)} \left[\left\| \mathbf{s}_\theta(\mathbf{x}(t), t) - \nabla_{\mathbf{x}(t)} \log p_{0t}(\mathbf{x}(t)|\mathbf{x}(0)) \right\|_2^2 \right] \right], \quad (4)$$

In this study, we follow DDPM Ho et al. [2020], which can be interpreted as a discretization of the VP-SDE:

$$d\mathbf{x} = -\frac{\beta(t)}{2}\mathbf{x}dt + \sqrt{\beta(t)}d\mathbf{w}, \quad (5)$$

where $\beta(t)$ is a noise schedule. For the discretization step, we adhere to the notational conventions defined by DDPM Ho et al. [2020]: $\mathbf{x}_i = \mathbf{x}(i/T)$, $\beta_i = \beta(i/T)$, $\alpha_i = 1 - \beta_i$, and $\bar{\alpha}_i = \prod_{k=1}^i \alpha_k$ for $i = 0, 1, \dots, T$.

2.2 Image Restoration by Conditional Diffusion

An Image Restoration is to recover an original image $\mathbf{x}_0 \in \mathbb{R}^n$ from a distorted version $\mathbf{y} \in \mathbb{R}^m$. In other words, we search for \mathbf{x}_0 such that

$$\mathbf{y} = \mathbf{A}\mathbf{x}_0 + \mathbf{n}, \quad (6)$$

where \mathbf{y} is a given noisy measurement degraded by a linear operator $\mathbf{A} : \mathbb{R}^n \rightarrow \mathbb{R}^m$ and a Gaussian noise $\mathbf{n} \sim \mathcal{N}(\mathbf{0}, \sigma^2 \mathbf{I})$. A conventional method for tackling this challenge entails optimizing the following objective function:

$$\arg \min_{\mathbf{x}} \|\mathbf{y} - \mathbf{A}\mathbf{x}\|_2^2 + \lambda \mathcal{R}(\mathbf{x}). \quad (7)$$

The first term of (7) is the data-fidelity term, which quantifies the pixel-level dissimilarities between the measurement and the distorted version of the generated image. Whereas the second term is regularization term.

Sampling of \mathbf{x}_0 given \mathbf{y} can be performed using the conditional generation of diffusion model Song et al. [2021]. The corresponding reverse SDE of (5) is given as follows:

$$d\mathbf{x} = \left[-\frac{\beta(t)}{2}\mathbf{x} - \beta(t)\nabla_{\mathbf{x}} \log p_t(\mathbf{x}|\mathbf{y}) \right] dt + \sqrt{\beta(t)}d\bar{\mathbf{w}}. \quad (8)$$

Adopting the convention of representing \mathbf{x}_t the value of \mathbf{x} at t , it follows from the Bayes' rule that the conditional score can be further decomposed into two terms:

$$\nabla_{\mathbf{x}_t} \log p_t(\mathbf{x}_t|\mathbf{y}) = \nabla_{\mathbf{x}_t} \log p_t(\mathbf{x}_t) + \nabla_{\mathbf{x}_t} \log p_t(\mathbf{y}|\mathbf{x}_t). \quad (9)$$

For the unconditional score $\nabla_{\mathbf{x}_t} \log p_t(\mathbf{x}_t)$, a pre-trained score approximator $\mathbf{s}_\theta(\mathbf{x}_t, t)$ can be used. Dhariwal and Nichol [2021a], Saharia et al. [2022] estimate the second term by training a model on paired data, whereas Diffusion Posterior Sampling (DPS) Chung et al. [2023] approximates it by $\nabla_{\mathbf{x}_t} \log p(\mathbf{y}|\hat{\mathbf{x}}_{0|t})$ where $\hat{\mathbf{x}}_{0|t}$ is the estimated posterior mean $\mathbb{E}[\mathbf{x}_0|\mathbf{x}_t]$, and hence

$$\nabla_{\mathbf{x}_t} \log p_t(\mathbf{y}|\mathbf{x}_t) \simeq -\frac{1}{\sigma^2} \nabla_{\mathbf{x}_t} \|\mathbf{y} - \mathbf{A}\hat{\mathbf{x}}_{0|t}\|_2^2. \quad (10)$$

3 Proposed Method

Existing approaches to inverse problems Chung et al. [2023], Zhu et al. [2023], Wang et al. [2022], Kawar et al. [2022a], Chung et al. [2022b] guide the generation process by minimizing the pixel-based data-fidelity term $\|\mathbf{y} - \mathbf{A}\mathbf{x}\|_2^2$, which does not consider the perceptual features of images. In this paper, we propose a modified data-fidelity term that incorporates spatial and frequency features through upsampling and Fourier transformation, respectively.

3.1 Modifying Data-fidelity

With the aim of enhancing the data-fidelity term, we replace term $\|\mathbf{y} - \mathbf{A}\mathbf{x}_0\|$ with term $\|\psi(\mathbf{y}) - \psi(\mathbf{A}\mathbf{x}_0)\|$ utilizing transformation ψ , which efficiently captures the perceptual characteristics of images.

To achieve satisfactory outcomes with this technique, it is recommended to carefully control the perturbation of the feasible solutions, aiming for minimal disruption. Fortunately, the validity of the following equation is well-established under the condition that ψ is injective.

$$\arg \min_{\mathbf{x}_0} \|\mathbf{y} - \mathbf{A}\mathbf{x}_0\| = \arg \min_{\mathbf{x}_0} \|\psi(\mathbf{y}) - \psi(\mathbf{A}\mathbf{x}_0)\| \quad (11)$$

Thus under the assumption of ψ 's injectivity, it is reasonable to expect that feasible solutions of (7) will be subjected to less disruption. Subsequently, we introduce an injective transformation ψ that effectively extracts perceptual features.

Spatial feature We propose to leverage the effect of upsampling images obtained via interpolation to incorporate not only pixel-level information but also the spatial context of the image. Image interpolation employs convolutional

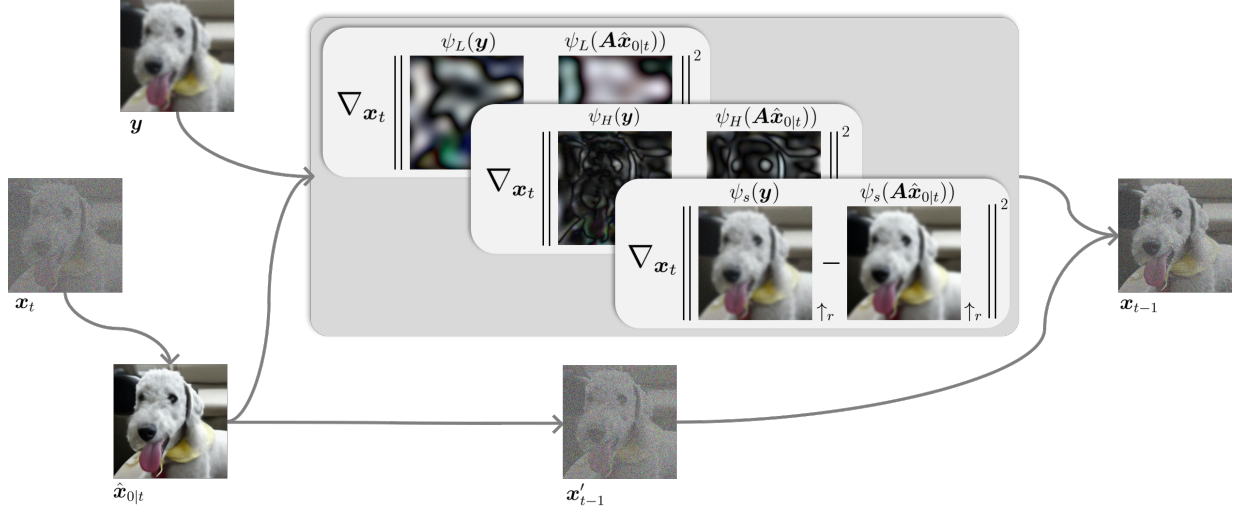


Figure 2: The overview of SaFaRI. Starting with the intermediate state x_t , we first generate the unconditional prediction $\hat{x}_{0|t}$ using the diffusion model. Then we obtain the next state x_{t-1} by leveraging the loss guidance terms obtained through bicubic upsampling ψ_s with scaling factor r , high-pass filter ψ_H and the low-pass filter ψ_L .

operations to compute the values of newly generated pixels. These values are determined through intricate interactions with neighboring pixels, effectively capturing the spatial context of the image.

In essence, the values of newly generated pixels can be interpreted as encapsulating crucial information derived from the surrounding spatial image patches. By doing so, we aim to enrich the overall representation of the image, leading to improved performance in various image processing tasks. In this paper, we employ the standard interpolation method, bicubic interpolation. We denote $\psi_{s,r}$ the bicubic upsampling with the ratio r . Note that the bicubic upsampling ψ_s is injective.

Frequency feature To enhance the alignment of the measurement with human perception, we incorporated the frequency domain representation of the image obtained through DFT. Employing its strength in extracting frequency information, the discrete Fourier transform (DFT) empowers the decomposition of the data-fidelity term into its low-frequency and high-frequency counterparts, providing a more detailed representation of the data.

Denote \mathcal{F} and \mathcal{F}^{-1} as the 2D discrete fourier transform (DFT) and its inverse transform, respectively. For an image $f \in \mathbb{R}^{M \times N \times C}$, the discrete Fourier transform \mathcal{F} decomposes f by the orthonormal basis with complex coefficients as follows:

$$\{\mathcal{F}(f)\}(u, v) = \sum_{i=0}^{M-1} \sum_{j=0}^{N-1} f(i, j) e^{-i2\pi(\frac{ui}{M} + \frac{vj}{N})} \quad (12)$$

for $(u, v) \in \mathbb{R}^M \times \mathbb{R}^N$. Our analysis builds upon channel-wise application of the DFT, henceforth represented without the channel dimension for conciseness.

We adopt the ideal highpass filtering and ideal lowpass filtering, denoted by H and L , as follows:

$$\{H(F)\}_{u,v} = \begin{cases} 0 & r(u, v) < r_0 \\ F_{u,v} & \text{otherwise} \end{cases} \quad (13)$$

$$\{L(F)\}_{u,v} = \begin{cases} F_{u,v} & r(u, v) < r_0 \\ 0 & \text{otherwise} \end{cases} \quad (14)$$

where $r(u, v) = \max\{|u - \frac{N}{2}|, |v - \frac{M}{2}|\}$.

Now we consider the transformation $\psi_f = (\psi_H^\top, \psi_L^\top)^\top$ where $\psi_H = \mathcal{F}^{-1} \circ H \circ \mathcal{F}$ and $\psi_L = \mathcal{F}^{-1} \circ L \circ \mathcal{F}$. The Parseval's theorem implies that ψ_f preserves 2-norm. Namely, denoting the difference $\mathbf{y} - \mathbf{A}\mathbf{x}_0$ as \mathbf{d} , $\|\psi_f(\mathbf{d})\|_2^2 = \|\mathbf{d}\|_2^2$ holds. Hence, ψ_f decomposes $\|\mathbf{d}\|_2^2$ to the high-frequency term $\|\psi_H(\mathbf{d})\|_2^2$ and the low-frequency term $\|\psi_L(\mathbf{d})\|_2^2$:

$$\|\mathbf{d}\|_2^2 = \|\psi_f(\mathbf{d})\|_2^2 = \|(\psi_H(\mathbf{d}), \psi_L(\mathbf{d}))\|_2^2 = \|\psi_H(\mathbf{d})\|_2^2 + \|\psi_L(\mathbf{d})\|_2^2 \quad (15)$$

Note that the operator ψ_f is norm-preserving operator, so ψ_f is injective. Also, that minimizing $\|\psi_H(\mathbf{d})\|_2^2$ and $\|\psi_L(\mathbf{d})\|_2^2$ implies minimizing the difference of high frequency features and low frequency features, respectively. Therefore, through adaptive weighting of the decomposed fidelity terms, we can selectively enhance the high-frequency components that play a critical role in visual perception.

3.2 Theoretical Analysis

While the approximation of $p_t(\mathbf{y}|\mathbf{x}_t)$ in Chung et al. [2023] is based on the assumption of a normal likelihood, the same principle can be extended to more general conditional probability distributions, represented by $\exp(-l_{\mathbf{y}}(\mathbf{x}_0))$ for some loss function $l_{\mathbf{y}}(\mathbf{x}_0)$ Graikos et al. [2022], Song et al. [2023]. In the context of this paper, we focus on the specific case of $l_{\psi, \mathbf{y}}(\mathbf{x}_0) = \frac{1}{2\gamma^2} \|\psi(\mathbf{y}) - \psi(\mathbf{A}\mathbf{x}_0)\|_2^2$

Same as Chung et al. [2023], we can factorize $p_t(\mathbf{y}|\mathbf{x}_t)$ as follows:

$$p_t(\mathbf{y}|\mathbf{x}_t) = \int p_t(\mathbf{y}|\mathbf{x}_0, \mathbf{x}_t)p(\mathbf{x}_0|\mathbf{x}_t)d\mathbf{x}_0 \quad (16)$$

$$= \int p(\mathbf{y}|\mathbf{x}_0)p(\mathbf{x}_0|\mathbf{x}_t)d\mathbf{x}_0 \quad (17)$$

Our approach is to modify $p(\mathbf{y}|\mathbf{x}_0)$ as $p_{\psi}(\mathbf{y}|\mathbf{x}_0)$:

$$p_{\psi}(\mathbf{y}|\mathbf{x}_0) = \frac{1}{Z_{\psi}} \exp \left[-\frac{1}{2\gamma^2} \|\psi(\mathbf{y}) - \psi(\mathbf{A}\mathbf{x}_0)\|_2^2 \right], \quad (18)$$

where Z_{ψ} is a normalizing constant. In that case, we factorize $p_{\psi, t}(\mathbf{y}|\mathbf{x}_t)$ by

$$p_{\psi, t}(\mathbf{y}|\mathbf{x}_t) = \int p_{\psi}(\mathbf{y}|\mathbf{x}_0)p(\mathbf{x}_0|\mathbf{x}_t)d\mathbf{x}_0 \quad (19)$$

Assuming that ψ is a linear operator, the distribution function $p_{\psi}(\mathbf{y}|\mathbf{x}_0)$ is Lipschitz continuous.

Lemma 1. *The modified conditional probability $p_{\psi}(\mathbf{y}|\mathbf{x}_0)$ defined as (18) is Lipschitz continuous with respect to \mathbf{x}_0 .*

Denote the posterior mean of $p(\mathbf{x}_t|\mathbf{x}_0)$ as $\hat{\mathbf{x}}_{0|t} = \mathbb{E}_{p(\mathbf{x}_0|\mathbf{x}_t)}[\mathbf{x}_0]$ where $p(\mathbf{x}_t|\mathbf{x}_0)$ is a DDPM forward process starting from time step 0. Then with similar argument in DPS Chung et al. [2023], the following holds:

Theorem 2. *For the given measurement \mathbf{y} , a linear operator ψ , a modified conditional probability $p_{\psi}(\mathbf{y}|\mathbf{x}_0) \propto \exp(-l_{\psi, \mathbf{y}}(\mathbf{x}_0))$, we can approximate $p_{\psi, t}(\mathbf{y}|\mathbf{x}_t)$ as follows:*

$$p_{\psi, t}(\mathbf{y}|\mathbf{x}_t) \simeq p_{\psi}(\mathbf{y}|\hat{\mathbf{x}}_{0|t}) \quad (20)$$

where the approximation error is bounded by

$$|p_{\psi, t}(\mathbf{y}|\mathbf{x}_t) - p_{\psi}(\mathbf{y}|\hat{\mathbf{x}}_{0|t})| \leq \frac{1}{e^{1/2}Z_{\psi}\gamma} \cdot L_{\psi} \cdot \|\mathbf{A}\| \cdot m_1 \quad (21)$$

where $m_1 := \int \|\mathbf{x}_0 - \hat{\mathbf{x}}_{0|t}\|p(\mathbf{x}_0|\mathbf{x}_t)d\mathbf{x}_0$, L_{ψ} is a Lipschitz constant of ψ and $\|\mathbf{A}\|$ is the operator norm associated to the Euclidean norm.

Furthermore, by the results of Theorem 2., we can approximate gradient of log likelihood with the analytically tractable term:

$$\nabla_{\mathbf{x}_t} \log p_{\psi, t}(\mathbf{y}|\mathbf{x}_t) \simeq \nabla_{\mathbf{x}_t} \log p_{\psi}(\mathbf{y}|\hat{\mathbf{x}}_{0|t}). \quad (22)$$

Remark 1. *Applying Tweedie's formula, one can prove that for the case of DDPM sampling, $\hat{\mathbf{x}}_{0|t}$ has the explicit representation:*

$$\hat{\mathbf{x}}_{0|t} = \frac{1}{\sqrt{\bar{\alpha}(t)}} (\mathbf{x}_t + (1 - \bar{\alpha}(t))\nabla_{\mathbf{x}_t} \log p_t(\mathbf{x}_t)) \quad (23)$$

Note that $p_{\psi, t}(\mathbf{y}, \hat{\mathbf{x}}_{0|t})$ is intractable in general. Despite the inherent complexity of the term, using the Theorem 2 and the equation 23, we can approximate it into an explicit form.

Algorithm 1 SaFaRI

Require:

Total number of iterations : T , measurement : \mathbf{y}
 Operators : $\psi_{s,r}, \psi_f = (\psi_H^\top, \psi_L^\top)^\top$
 Hyperparameters : $\tau, \{\rho_t^s, \rho_t^H, \rho_t^L\}_{t=1}^T, \{\tilde{\sigma}_t\}_{t=1}^T$

- 1: $\mathbf{x}_T \sim \mathcal{N}(\mathbf{0}, \mathbf{I})$
- 2: **for** $t = T$ **to** 1 **do**
- 3: $\psi_s \leftarrow \psi_{s,r}$
- 4: **if** $t > \tau$ **then**
- 5: $\psi_s \leftarrow \text{identity}$
- 6: **end if**
- 7: $\hat{\mathbf{x}}_{0|t} \leftarrow \frac{1}{\sqrt{\bar{\alpha}_t}} (\mathbf{x}_t + (1 - \bar{\alpha}_t) \mathbf{s}_\theta(\mathbf{x}_t, t))$
- 8: **if** $t > 1$ **then**
- 9: $\mathbf{z} \sim \mathcal{N}(\mathbf{0}, \mathbf{I})$
- 10: **else**
- 11: $\mathbf{z} = \mathbf{0}$
- 12: **end if**
- 13: $\mathbf{x}'_{t-1} \leftarrow \frac{\sqrt{\bar{\alpha}_t(1-\bar{\alpha}_{t-1})}}{1-\bar{\alpha}_t} \mathbf{x}_t + \frac{\sqrt{\bar{\alpha}_{t-1}\beta_t}}{1-\bar{\alpha}_t} \hat{\mathbf{x}}_{0|t} + \tilde{\sigma}_t \mathbf{z}$
- 14: $\mathcal{L}_s \leftarrow \|\psi_s(\mathbf{y}) - \psi_s(\mathbf{A}(\hat{\mathbf{x}}_{0|t}))\|_2^2$
- 15: $\mathcal{L}_H \leftarrow \|\psi_H(\mathbf{y}) - \psi_H(\mathbf{A}(\hat{\mathbf{x}}_{0|t}))\|_2^2$
- 16: $\mathcal{L}_L \leftarrow \|\psi_L(\mathbf{y}) - \psi_L(\mathbf{A}(\hat{\mathbf{x}}_{0|t}))\|_2^2$
- 17: $\mathbf{x}_{t-1} \leftarrow \mathbf{x}'_{t-1} - \rho_t^s \nabla_{\mathbf{x}_t} \mathcal{L}_s - \rho_t^H \nabla_{\mathbf{x}_t} \mathcal{L}_H - \rho_t^L \nabla_{\mathbf{x}_t} \mathcal{L}_L$
- 18: **end for**
- 19: **return** \mathbf{x}_0

3.3 SaFaRI

Leveraging the synergistic power of the preceding concepts, we propose **SaFaRI**: Spatial-and-Frequency-aware Restoration method for Images, a novel methodology that tailors the data-fidelity term to spatial and frequency domains, enabling a more comprehensive representation of the underlying perceptual attributes of the images.

In order to consider both spatial and frequency features, we consider the data-fidelity with respect to $\psi = (\psi_s^\top, \psi_f^\top)^\top$. Since both ψ_s and ψ_f are injective, ψ is also injective. Owing to its injective nature, ψ is expected to cause minimal disruption to feasible solutions of (7). In this case, it is represented as follow:

$$\begin{aligned}
 \|\psi(\mathbf{y}) - \psi(\mathbf{A}\hat{\mathbf{x}}_{0|t})\|_2^2 &= \|\psi_s(\mathbf{y}) - \psi_s(\mathbf{A}\hat{\mathbf{x}}_{0|t})\|_2^2 \\
 &\quad + \|\psi_H(\mathbf{y}) - \psi_H(\mathbf{A}\hat{\mathbf{x}}_{0|t})\|_2^2 \\
 &\quad + \|\psi_L(\mathbf{y}) - \psi_L(\mathbf{A}\hat{\mathbf{x}}_{0|t})\|_2^2.
 \end{aligned} \tag{24}$$

To enhance the algorithm's stability, in practice, we fix τ and set ψ_s to identity for first $T - \tau$ iterations where T is the total number of iterations. Additionally, To optimize its performance, we carefully adjusted the weights of the three data-fidelity terms: spatial-aware term ρ_t^s , high-frequency term ρ_t^H , and low-frequency term ρ_t^L . A detailed algorithmic formulation of SaFaRI is presented in Algorithm 1. Choices of operators and hyperparameters are in Appendix. For the visual representation of SaFaRI, please refer to Figure 2.

4 Experiments

4.1 Implementation Details

To benchmark the proposed method against existing approaches, we conduct a comparative study using ImageNet 256×256 Deng et al. [2009] and FFHQ 256×256 Karras et al. [2019] datasets. For each dataset, we evaluate 1k validation images. We leveraged the pre-trained diffusion models for ImageNet and FFHQ datasets taken from Dhariwal and Nichol [2021b] and Chung et al. [2023], respectively, without any adjustments. All images are normalized to the range $[0, 1]$.

Method	Inpaint (random)		Inpaint (box)		Deblur (Gauss)		SR ($\times 4$)	
	LPIPS \downarrow	FID \downarrow	LPIPS \downarrow	FID \downarrow	LPIPS \downarrow	FID \downarrow	LPIPS \downarrow	FID \downarrow
DPS Chung et al. [2023]	0.350	15.809	0.350	57.584	0.398	49.480	0.324	41.090
DiffPIR Zhu et al. [2023]	0.141	15.216	0.255	47.210	0.336	39.502	0.351	44.176
PnP-ADMM Chan et al. [2016]	0.414	78.639	0.395	125.608	0.501	101.900	0.389	66.539
ILVR Choi et al. [2021]	0.352	48.419	0.315	61.083	0.477	80.369	0.441	74.364
SaFaRI (ours)	0.124	10.477	<u>0.204</u>	38.160	0.311	34.460	<u>0.296</u>	31.258
SaFaRI-spatial (ours)	<u>0.127</u>	<u>11.317</u>	0.214	40.668	<u>0.312</u>	<u>34.705</u>	0.307	33.315
SaFaRI-freq. (ours)	<u>0.129</u>	12.319	0.199	<u>38.358</u>	0.317	35.160	0.295	<u>31.284</u>

Table 1: Quantitative evaluation of image restoration task with Gaussian noise ($\sigma = 0.025$) on ImageNet 256×256 -1k validation dataset. We compare our method with other zero-shot IR methods. We compute the metrics LPIPS and FID for various tasks. **Bold**: Best, under: second best. (The ranking was done before the rounding)

Method	Inpaint (random)		Inpaint (box)		Deblur (Gauss)		SR ($\times 4$)	
	LPIPS \downarrow	FID \downarrow	LPIPS \downarrow	FID \downarrow	LPIPS \downarrow	FID \downarrow	LPIPS \downarrow	FID \downarrow
DPS Chung et al. [2023]	0.099	12.766	0.147	20.885	0.211	23.152	0.200	<u>21.060</u>
DiffPIR Zhu et al. [2023]	0.130	18.788	0.199	22.963	0.213	22.124	0.236	25.192
PnP-ADMM Chan et al. [2016]	0.466	119.409	0.451	155.291	0.392	69.767	0.290	50.679
ILVR Choi et al. [2021]	0.245	39.202	0.272	32.640	0.316	51.153	0.315	49.227
SaFaRI (ours)	0.089	9.014	0.106	12.486	0.203	22.046	0.200	20.977
SaFaRI-spatial (ours)	0.098	10.954	0.130	14.338	0.206	22.567	0.204	21.938
SaFaRI-freq. (ours)	<u>0.091</u>	<u>9.800</u>	<u>0.126</u>	<u>13.000</u>	<u>0.203</u>	<u>22.083</u>	<u>0.200</u>	21.242

Table 2: Quantitative evaluation of image restoration task with Gaussian noise ($\sigma = 0.025$) on FFHQ 256×256 -1k validation dataset. We compare our method with other zero-shot IR methods. We compute the metrics LPIPS Zhang et al. [2018] and FID Heusel et al. [2017] for various tasks. **Bold**: Best, under: second best. (The ranking was done before the rounding)

We conducted experiments using four different degradation tasks. For inpainting, we utilize two mask type; box-type mask and random-type mask. For random-type mask, we mask out 92% of the total pixels, and for box-type mask, we mask out 128×128 box region randomly, following Chung et al. [2023]. For gaussian deblur, we use 61×61 gaussian blur kernel with standard deviation of 3.0. Lastly, For super-resolution, bicubic downsampling is performed. For all tasks, we add gaussian noise to the measurement with standard deviation of 0.025. Additional experimental details are provided in Appendix.

4.2 Quantitative Experiments

To objectively assess the perceptual similarity between two images, we employ two widely recognized metrics: Fréchet Inception Distance (FID) and Learned Perceptual Image Patch Similarity (LPIPS). For comprehensive evaluation, additional objective metrics such as peak signal-to-noise ratio (PSNR) and structural similarity index (SSIM) are presented in the Appendix.

We test our approaches with the following methods: Denoising diffusion models for plug-and-play image restoration (DiffPIR) Zhu et al. [2023], Diffusion posterior sampling for general noisy inverse problems (DPS) Chung et al. [2023], Plug-and-play alternating direction method of multipliers (PnP-ADMM) Chan et al. [2016] using DnCNN Zhang et al. [2017] instead of proximal mappings, Iterative latent variable refinement (ILVR) Choi et al. [2021]. Although ILVR only deals with super-resolution task, we adopted projections onto convex sets (POCS) method Chung et al. [2023] for inpainting Song et al. [2021] and Gaussian deblurring task. In the case of DiffPIR, we used the case with NFEs of 100 for the experiments. We additionally evaluate SaFaRI-spatial and SaFaRI-frequency, which are SaFaRI methods with $\psi_f = 0$ and $\psi_s = 0$ respectively. To ensure a fair comparison, same pre-trained score function are used for all diffusion model-based methods in the experiments.

We present the quantitative results for ImageNet dataset in Table 1 and results for FFHQ dataset in Table 2. Our method establishes a new state-of-the-art benchmark for image restoration performance, consistently outperforming other zero-shot based methods across both datasets and all image restoration tasks. In particular, our method achieved

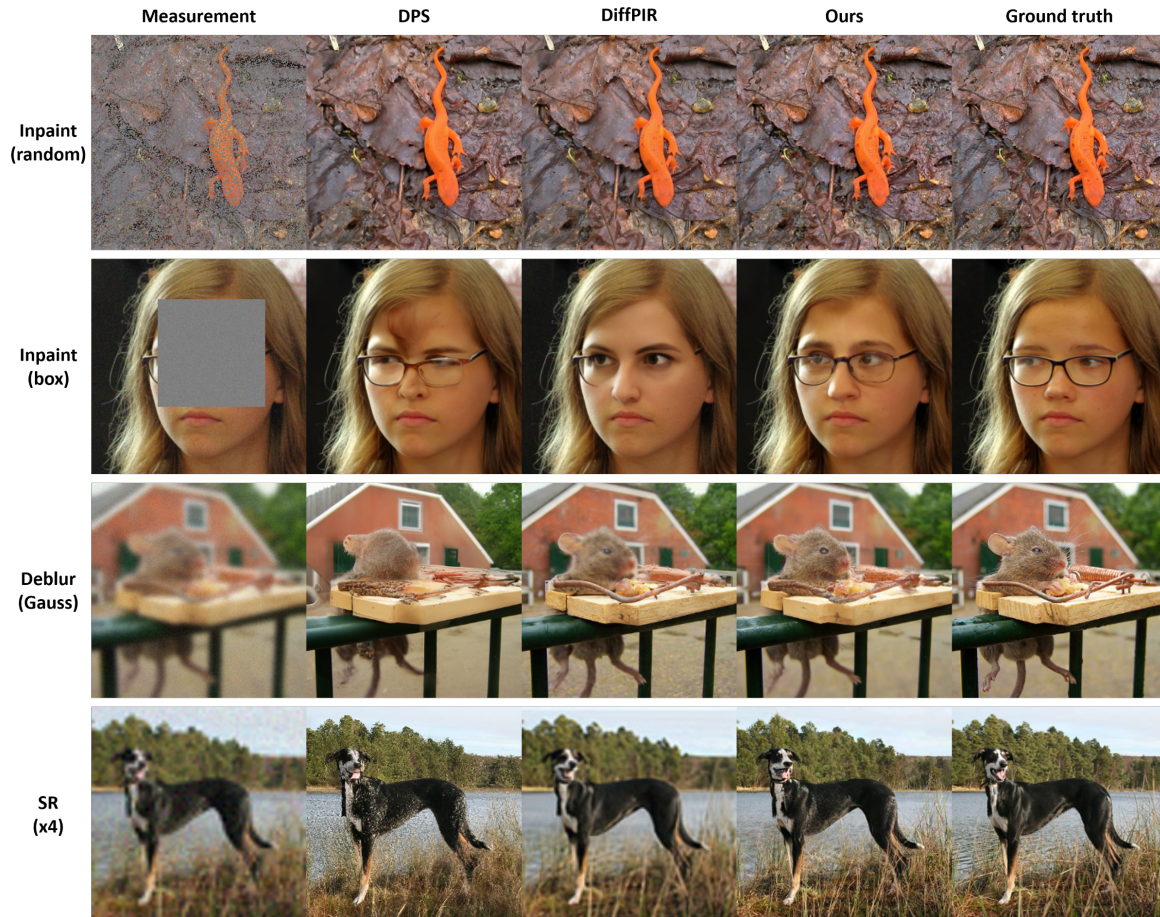


Figure 3: Qualitative results of image restoration. We establish the efficacy of SaFaRI in restoring images across a variety of tasks.

significantly better results than previous methods on the ImageNet dataset, where the data prior is more complex and conditional guiding is more important. Furthermore, the utilization of either spatial or frequency alone is sufficient for our method to outperform existing methods, demonstrating our approach’s superior capabilities and effectiveness.

4.3 Qualitative Experiments

Figure 1 illustrates the superior performance of our proposed approach. Also, figure 3 provides a comprehensive comparison of SaFaRI against DPS and DiffPIR on a variety of IR tasks, encompassing inpainting with random and box masks, Gaussian deblurring, and super-resolution ($\times 4$). Our method consistently surpasses the benchmarks, generating high-quality reconstructions that exhibit remarkable perceptual context alignment.

For random-type inpainting, previous methods also generate sufficiently good images, but our method better restores semantic features. A comparison of the first row of Fig 3 with results obtained from other methods clearly highlights the superior performance of our method in generating highly detailed and realistic representations of the surrounding environment and the lizard’s skin. Also, despite the inherent complexities of box inpainting, our approach successfully generates realistic and seamlessly integrated glasses occluded by the mask, resulting in natural-looking images with imperceptible boundaries between the masked and unmasked regions. In addition, our approach successfully deblurs the measurements, leading to the faithful reconstruction of intricate features, such as the eyes and fur texture. Moreover, in the context of super-resolution applications, our method excels at reconstructing high-quality images that maintain the integrity of both foreground objects and background elements.

Overall, SaFaRI can effectively capture and preserve fine-grained texture information, resulting in more realistic and visually appealing images.

5 Conclusion

This paper presents **SaFaRI**, a novel diffusion model-based image restoration approach that incorporates spatial and frequency information into the data fidelity term, effectively enhancing the restoration performance. By leveraging both spatial and frequency via bicubic upsampling and Fourier transformation, **SaFaRI** achieves state-of-the-art results on a variety of image restoration benchmarks, outperforming existing methods.

Despite the remarkable performance of our proposed methodology, the application of the transformation inevitably induces perturbations to the feasible solutions due to the influence of the prior term. A comprehensive analysis of the solution perturbations can strengthen the theoretical foundation of our methodology.

References

- Leonid I Rudin, Stanley Osher, and Emad Fatemi. Nonlinear total variation based noise removal algorithms. *Physica D: nonlinear phenomena*, 60(1-4):259–268, 1992.
- Martin Benning and Martin Burger. Modern regularization methods for inverse problems. *Acta numerica*, 27:1–111, 2018.
- Jonathan Ho, Ajay Jain, and Pieter Abbeel. Denoising diffusion probabilistic models. *Advances in neural information processing systems*, 33:6840–6851, 2020.
- Yang Song, Jascha Sohl-Dickstein, Diederik P Kingma, Abhishek Kumar, Stefano Ermon, and Ben Poole. Score-based generative modeling through stochastic differential equations. In *International Conference on Learning Representations*, 2021. URL <https://openreview.net/forum?id=PXTIG12RRHS>.
- Prafulla Dhariwal and Alexander Nichol. Diffusion models beat gans on image synthesis. *Advances in neural information processing systems*, 34:8780–8794, 2021a.
- Jooyoung Choi, Sungwon Kim, Yonghyun Jeong, Youngjune Gwon, and Sungroh Yoon. Ilvr: Conditioning method for denoising diffusion probabilistic models. *arXiv preprint arXiv:2108.02938*, 2021.
- Bahjat Kawar, Gregory Vaksman, and Michael Elad. SNIPS: Solving noisy inverse problems stochastically. *Advances in Neural Information Processing Systems*, 34:21757–21769, 2021.
- Bahjat Kawar, Michael Elad, Stefano Ermon, and Jiaming Song. Denoising diffusion restoration models. *Advances in Neural Information Processing Systems*, 35:23593–23606, 2022a.
- Yinhuai Wang, Jiwen Yu, and Jian Zhang. Zero-shot image restoration using denoising diffusion null-space model. *arXiv preprint arXiv:2212.00490*, 2022.
- Hyungjin Chung, Jeongsol Kim, Michael Thompson Mccann, Marc Louis Klasky, and Jong Chul Ye. Diffusion posterior sampling for general noisy inverse problems. In *The Eleventh International Conference on Learning Representations*, 2023. URL <https://openreview.net/forum?id=0nD9zGAGT0k>.
- Yuanzhi Zhu, Kai Zhang, Jingyun Liang, Jiezhong Cao, Bihan Wen, Radu Timofte, and Luc Van Gool. Denoising diffusion models for plug-and-play image restoration. In *IEEE Conference on Computer Vision and Pattern Recognition Workshops (NTIRE)*, 2023.
- Hyungjin Chung, Byeongsu Sim, and Jong Chul Ye. Come-closer-diffuse-faster: Accelerating conditional diffusion models for inverse problems through stochastic contraction. In *Proceedings of the IEEE/CVF Conference on Computer Vision and Pattern Recognition*, pages 12413–12422, 2022a.
- Hyungjin Chung, Byeongsu Sim, Dohoon Ryu, and Jong Chul Ye. Improving diffusion models for inverse problems using manifold constraints. *Advances in Neural Information Processing Systems*, 35:25683–25696, 2022b.
- Jiaming Song, Arash Vahdat, Morteza Mardani, and Jan Kautz. Pseudoinverse-guided diffusion models for inverse problems. In *International Conference on Learning Representations*, 2022.
- Andreas Lugmayr, Martin Danelljan, Andres Romero, Fisher Yu, Radu Timofte, and Luc Van Gool. Repaint: Inpainting using denoising diffusion probabilistic models. In *Proceedings of the IEEE/CVF Conference on Computer Vision and Pattern Recognition*, pages 11461–11471, 2022.
- Ben Fei, Zhaoyang Lyu, Liang Pan, Junzhe Zhang, Weidong Yang, Tianyue Luo, Bo Zhang, and Bo Dai. Generative diffusion prior for unified image restoration and enhancement. In *Proceedings of the IEEE/CVF Conference on Computer Vision and Pattern Recognition*, pages 9935–9946, 2023.
- Bahjat Kawar, Jiaming Song, Stefano Ermon, and Michael Elad. Jpeg artifact correction using denoising diffusion restoration models. *arXiv preprint arXiv:2209.11888*, 2022b.

- Hong Chen and Gary E Ford. Perceptual wiener filtering for image restoration. In *Proceedings of 1994 28th Asilomar Conference on Signals, Systems and Computers*, volume 1, pages 218–222. IEEE, 1994.
- Jireh Jam, Connah Kendrick, Vincent Drouard, Kevin Walker, Gee-Sern Hsu, and Moi Hoon Yap. R-mnet: A perceptual adversarial network for image inpainting. In *Proceedings of the IEEE/CVF Winter Conference on Applications of Computer Vision*, pages 2714–2723, 2021.
- Rastislav Lukac. *Perceptual digital imaging: methods and applications*. CRC Press, 2017.
- Chaoyue Wang, Chang Xu, Chaohui Wang, and Dacheng Tao. Perceptual adversarial networks for image-to-image transformation. *IEEE Transactions on Image Processing*, 27(8):4066–4079, 2018.
- Wenhan Yang, Shiqi Wang, Yuming Fang, Yue Wang, and Jiaying Liu. From fidelity to perceptual quality: A semi-supervised approach for low-light image enhancement. In *Proceedings of the IEEE/CVF conference on computer vision and pattern recognition*, pages 3063–3072, 2020.
- Haichuan Ma, Dong Liu, and Feng Wu. Rectified wasserstein generative adversarial networks for perceptual image restoration. *IEEE Transactions on Pattern Analysis and Machine Intelligence*, 45(3):3648–3663, 2022.
- Leida Li, Ya Yan, Yuming Fang, Shiqi Wang, Lu Tang, and Jiansheng Qian. Perceptual quality evaluation for image defocus deblurring. *Signal Processing: Image Communication*, 48:81–91, 2016.
- Xingyi Yang, Daquan Zhou, Jiashi Feng, and Xinchao Wang. Diffusion probabilistic model made slim. In *Proceedings of the IEEE/CVF Conference on Computer Vision and Pattern Recognition*, pages 22552–22562, 2023.
- Xin Yuan, Linjie Li, Jianfeng Wang, Zhengyuan Yang, Kevin Lin, Zicheng Liu, and Lijuan Wang. Spatial-frequency u-net for denoising diffusion probabilistic models. *arXiv preprint arXiv:2307.14648*, 2023.
- Zehua Sheng, Xiongwei Liu, Si-Yuan Cao, Hui-Liang Shen, and Huaqi Zhang. Frequency-domain deep guided image denoising. *IEEE Transactions on Multimedia*, 2022.
- Dario Fuoli, Luc Van Gool, and Radu Timofte. Fourier space losses for efficient perceptual image super-resolution. In *Proceedings of the IEEE/CVF International Conference on Computer Vision*, pages 2360–2369, 2021.
- Seyed Mehdi Ayyoubzadeh and Xiaolin Wu. High frequency detail accentuation in cnn image restoration. *IEEE Transactions on Image Processing*, 30:8836–8846, 2021.
- Mingwen Shao, Yuanjian Qiao, Deyu Meng, and Wangmeng Zuo. Uncertainty-guided hierarchical frequency domain transformer for image restoration. *Knowledge-Based Systems*, 263:110306, 2023.
- Brian D.O. Anderson. Reverse-time diffusion equation models. *Stochastic Processes and their Applications*, 12(3): 313–326, May 1982. URL <https://ideas.repec.org/a/eee/spapps/v12y1982i3p313-326.html>.
- Yang Song and Stefano Ermon. Generative modeling by estimating gradients of the data distribution. In *Advances in Neural Information Processing Systems*, pages 11895–11907, 2019.
- Chitwan Saharia, Jonathan Ho, William Chan, Tim Salimans, David J Fleet, and Mohammad Norouzi. Image super-resolution via iterative refinement. *IEEE Transactions on Pattern Analysis and Machine Intelligence*, 45(4): 4713–4726, 2022.
- Alexandros Graikos, Nikolay Malkin, Nebojsa Jojic, and Dimitris Samaras. Diffusion models as plug-and-play priors. *Advances in Neural Information Processing Systems*, 35:14715–14728, 2022.
- Jiaming Song, Qinsheng Zhang, Hongxu Yin, Morteza Mardani, Ming-Yu Liu, Jan Kautz, Yongxin Chen, and Arash Vahdat. Loss-guided diffusion models for plug-and-play controllable generation. In Andreas Krause, Emma Brunskill, Kyunghyun Cho, Barbara Engelhardt, Sivan Sabato, and Jonathan Scarlett, editors, *Proceedings of the 40th International Conference on Machine Learning*, volume 202 of *Proceedings of Machine Learning Research*, pages 32483–32498. PMLR, 23–29 Jul 2023. URL <https://proceedings.mlr.press/v202/song23k.html>.
- Stanley H Chan, Xiran Wang, and Omar A Elgendy. Plug-and-play admn for image restoration: Fixed-point convergence and applications. *IEEE Transactions on Computational Imaging*, 3(1):84–98, 2016.
- Richard Zhang, Phillip Isola, Alexei A Efros, Eli Shechtman, and Oliver Wang. The unreasonable effectiveness of deep features as a perceptual metric. In *Proceedings of the IEEE conference on computer vision and pattern recognition*, pages 586–595, 2018.
- Martin Heusel, Hubert Ramsauer, Thomas Unterthiner, Bernhard Nessler, and Sepp Hochreiter. Gans trained by a two time-scale update rule converge to a local nash equilibrium. *Advances in neural information processing systems*, 30, 2017.
- Jia Deng, Wei Dong, Richard Socher, Li-Jia Li, Kai Li, and Li Fei-Fei. Imagenet: A large-scale hierarchical image database. In *2009 IEEE conference on computer vision and pattern recognition*, pages 248–255. Ieee, 2009.

- Tero Karras, Samuli Laine, and Timo Aila. A style-based generator architecture for generative adversarial networks. In *Proceedings of the IEEE/CVF conference on computer vision and pattern recognition*, pages 4401–4410, 2019.
- Prafulla Dhariwal and Alexander Nichol. Diffusion models beat gans on image synthesis. *Advances in neural information processing systems*, 34:8780–8794, 2021b.
- Kai Zhang, Wangmeng Zuo, Yunjin Chen, Deyu Meng, and Lei Zhang. Beyond a gaussian denoiser: Residual learning of deep cnn for image denoising. *IEEE transactions on image processing*, 26(7):3142–3155, 2017.

Supplementary Material

A Proofs

Lemma 1. *The modified conditional probability $p_\psi(\mathbf{y}|\mathbf{x}_0)$ defined as (18) is Lipschitz continuous with respect to \mathbf{x}_0 .*

Proof. Let $h(\mathbf{z}) := \frac{1}{Z_\psi} \exp\left[-\frac{1}{2\gamma^2}\|\mathbf{z} - \psi(\mathbf{y})\|_2^2\right]$, then the modified conditional distribution $p_\psi(\mathbf{y}|\mathbf{x}_0)$ is a composition of h , ψ and \mathbf{A} . Since ψ and \mathbf{A} are both linear, it suffices to show that h is Lipschitz continuous. Since

$$\frac{\partial}{\partial \mathbf{z}_i} h(\mathbf{z}) = \frac{1}{Z_\psi} \cdot \left(-\frac{\mathbf{z}_i - \psi(\mathbf{y})_i}{\gamma^2}\right) \cdot \exp\left[-\frac{1}{2\gamma^2}\|\mathbf{z} - \psi(\mathbf{y})\|_2^2\right], \quad (25)$$

$$\frac{\partial^2}{\partial \mathbf{z}_i^2} h(\mathbf{z}) = \frac{1}{Z_\psi \gamma^2} \cdot \left[\frac{(\mathbf{z}_i - \psi(\mathbf{y})_i)^2}{\gamma^2} - 1\right] \cdot \exp\left[-\frac{1}{2\gamma^2}\|\mathbf{z} - \psi(\mathbf{y})\|_2^2\right], \quad (26)$$

for each \mathbf{z}_i , $\left|\frac{\partial h}{\partial \mathbf{z}_i}\right|$ attains maximum $\frac{1}{e^{1/2} Z_\psi \gamma}$ at $\mathbf{z}_i = \psi(\mathbf{y})_i \pm \gamma$. Thus we have

$$|h(\mathbf{z}_1) - h(\mathbf{z}_2)| \leq \sup_{\mathbf{z}} \|\nabla h(\mathbf{z})\|_\infty \cdot \|\mathbf{z}_1 - \mathbf{z}_2\| \quad (27)$$

$$\leq \sup_{\mathbf{z}} \max_i \left|\frac{\partial h}{\partial \mathbf{z}_i}\right| \cdot \|\mathbf{z}_1 - \mathbf{z}_2\| \quad (28)$$

$$\leq \frac{1}{e^{1/2} Z_\psi \gamma} \|\mathbf{z}_1 - \mathbf{z}_2\|, \quad (29)$$

which shows that h is Lipschitz continuous and consequently $p_\psi(\mathbf{y}|\mathbf{x}_0)$ is also Lipschitz continuous. Note that the Lipschitz constant of $p_\psi(\mathbf{y}|\mathbf{x}_0)$ is the product of all Lipschitz constants of h , ψ and \mathbf{A} . \square

Employing the aforementioned above lemma, we can derive the following theorem:

Theorem 2. *For the given measurement \mathbf{y} , a linear operator ψ , a modified conditional probability $p_\psi(\mathbf{y}|\mathbf{x}_0) \propto \exp(-l_{\psi, \mathbf{y}}(\mathbf{x}_0))$, we can approximate $p_{\psi, t}(\mathbf{y}|\mathbf{x}_t)$ as follows:*

$$p_{\psi, t}(\mathbf{y}|\mathbf{x}_t) \simeq p_\psi(\mathbf{y}|\hat{\mathbf{x}}_{0|t}) \quad (20)$$

where the approximation error is bounded by

$$|p_{\psi, t}(\mathbf{y}|\mathbf{x}_t) - p_\psi(\mathbf{y}|\hat{\mathbf{x}}_{0|t})| \leq \frac{1}{e^{1/2} Z_\psi \gamma} \cdot L_\psi \cdot \|\mathbf{A}\| \cdot m_1 \quad (21)$$

where $m_1 := \int \|\mathbf{x}_0 - \hat{\mathbf{x}}_{0|t}\| p(\mathbf{x}_0|\mathbf{x}_t) d\mathbf{x}_0$, L_ψ is a Lipschitz constant of ψ and $\|\mathbf{A}\|$ is the operator norm associated to the Euclidean norm.

Proof. It follows from the above lemma that $p_\psi(\mathbf{y}|\mathbf{x}_0)$ is Lipschitz continuous with Lipschitz constant $\frac{1}{e^{1/2} Z_\psi \gamma} \cdot L_\psi \cdot \|\mathbf{A}\|$. Therefore, the error bound is

$$|p_{\psi, t}(\mathbf{y}|\mathbf{x}_t) - p_\psi(\mathbf{y}|\hat{\mathbf{x}}_{0|t})| = \left| \int p_\psi(\mathbf{y}|\mathbf{x}_0) p(\mathbf{x}_0|\mathbf{x}_t) d\mathbf{x}_0 - p_\psi(\mathbf{y}|\hat{\mathbf{x}}_{0|t}) \right| \quad (30)$$

$$= \left| \int (p_\psi(\mathbf{y}|\mathbf{x}_0) - p_\psi(\mathbf{y}|\hat{\mathbf{x}}_{0|t})) p(\mathbf{x}_0|\mathbf{x}_t) d\mathbf{x}_0 \right| \quad (31)$$

$$\leq \int |(p_\psi(\mathbf{y}|\mathbf{x}_0) - p_\psi(\mathbf{y}|\hat{\mathbf{x}}_{0|t}))| p(\mathbf{x}_0|\mathbf{x}_t) d\mathbf{x}_0 \quad (32)$$

$$\leq \frac{1}{e^{1/2} Z_\psi \gamma} \cdot L_\psi \cdot \|\mathbf{A}\| \cdot \int \|\mathbf{x}_0 - \hat{\mathbf{x}}_{0|t}\| p(\mathbf{x}_0|\mathbf{x}_t) d\mathbf{x}_0 \quad (33)$$

$$= \frac{1}{e^{1/2} Z_\psi \gamma} \cdot L_\psi \cdot \|\mathbf{A}\| \cdot m_1, \quad (34)$$

where the second last line comes from the Lipschitz continuity. \square

B Experimental Details

B.1 Hyperparameter setting

We provide a comprehensive overview of the hyperparameter configurations utilized for our algorithm in each problem setting. For spatial feature operator $\psi_{s,r}$, bicubic upsampling with a factor of $r = 4$ has been used throughout all experiments. Table 3 and Table 4 shows the values for the hyperparameters for each task on ImageNet and FFHQ respectively.

	Inpainting (random)	Inpainting (box)	Deblur (Gauss)	SR ($\times 4$)
r_0	5	5	4	5
τ	0.7	0.5	0.5	0.7
$\rho_{t>\tau}^H$	$0.0 / \sqrt{\mathcal{L}_H}$	$0.125 / \sqrt{\mathcal{L}_H}$	$0.0125 / \sqrt{\mathcal{L}_H}$	$0.25 / \sqrt{\mathcal{L}_H}$
$\rho_{t>\tau}^L$	$0.0 / \sqrt{\mathcal{L}_L}$	$0.125 / \sqrt{\mathcal{L}_L}$	$0.025 / \sqrt{\mathcal{L}_L}$	$0.25 / \sqrt{\mathcal{L}_L}$
$\rho_{t>\tau}^s$	$0.25 / \sqrt{\mathcal{L}_s}$	$0.125 / \sqrt{\mathcal{L}_s}$	$0.075 / \sqrt{\mathcal{L}_s}$	$0.025 / \sqrt{\mathcal{L}_s}$
$\rho_{t\leq\tau}^H$	$0.125 / \sqrt{\mathcal{L}_H}$	$0.625 / \sqrt{\mathcal{L}_H}$	$0.3 / \sqrt{\mathcal{L}_H}$	$1.25 / \sqrt{\mathcal{L}_H}$
$\rho_{t\leq\tau}^L$	$0.025 / \sqrt{\mathcal{L}_L}$	$0.125 / \sqrt{\mathcal{L}_L}$	$0.15 / \sqrt{\mathcal{L}_L}$	$0.25 / \sqrt{\mathcal{L}_L}$
$\rho_{t\leq\tau}^s$	$0.35 / \sqrt{\mathcal{L}_s}$	$0.125 / \sqrt{\mathcal{L}_s}$	$0.225 / \sqrt{\mathcal{L}_s}$	$0.0 / \sqrt{\mathcal{L}_s}$

Table 3: Hyperparameters of image restoration tasks on ImageNet 256×256 dataset.

	Inpainting (random)	Inpainting (box)	Deblur (Gauss)	SR ($\times 4$)
r_0	5	5	5	2
τ	0.7	0.5	0.7	0.7
$\rho_{t>\tau}^H$	$0.2 / \sqrt{\mathcal{L}_H}$	$0.125 / \sqrt{\mathcal{L}_H}$	$0.25 / \sqrt{\mathcal{L}_H}$	$0.15 / \sqrt{\mathcal{L}_H}$
$\rho_{t>\tau}^L$	$0.2 / \sqrt{\mathcal{L}_L}$	$0.125 / \sqrt{\mathcal{L}_L}$	$0.25 / \sqrt{\mathcal{L}_L}$	$0.15 / \sqrt{\mathcal{L}_L}$
$\rho_{t>\tau}^s$	$0.075 / \sqrt{\mathcal{L}_s}$	$0.05 / \sqrt{\mathcal{L}_s}$	$0.05 / \sqrt{\mathcal{L}_s}$	$0.1 / \sqrt{\mathcal{L}_s}$
$\rho_{t\leq\tau}^H$	$0.8 / \sqrt{\mathcal{L}_H}$	$0.75 / \sqrt{\mathcal{L}_H}$	$1.25 / \sqrt{\mathcal{L}_H}$	$1.0 / \sqrt{\mathcal{L}_H}$
$\rho_{t\leq\tau}^L$	$0.2 / \sqrt{\mathcal{L}_L}$	$0.375 / \sqrt{\mathcal{L}_L}$	$0.25 / \sqrt{\mathcal{L}_L}$	$0.25 / \sqrt{\mathcal{L}_L}$
$\rho_{t\leq\tau}^s$	$0.15 / \sqrt{\mathcal{L}_s}$	$0.1 / \sqrt{\mathcal{L}_s}$	$0.025 / \sqrt{\mathcal{L}_s}$	$0.0 / \sqrt{\mathcal{L}_s}$

Table 4: Hyperparameters of image restoration tasks on FFHQ 256×256 dataset.

In addition, for the Super Resolution task employing the FFHQ dataset, we utilize an upsampling operator in place of the identity operator for ψ_s .

B.2 Comparison methods

DPS The default configuration in DPS Chung et al. [2023] was employed for all experiments, except for a few tasks. Given the enhanced performance of the new setting for both Gaussian deblurring(GB) and box-mask inpainting(IB) tasks on the ImageNet dataset, we opted to adopt this configuration for subsequent experiments. In this regard, we established the hyperparameter as follows:

$$\zeta_i = \begin{cases} 0.15 / \|\mathbf{y} - \mathbf{A}(\hat{\mathbf{x}}_{0|t}(\mathbf{x}_i))\| & \text{Deblur (Gauss), ImageNet dataset} \\ 0.25 / \|\mathbf{y} - \mathbf{A}(\hat{\mathbf{x}}_{0|t}(\mathbf{x}_i))\| & \text{Inpainting (box), ImageNet dataset} \end{cases} \quad (35)$$

DiffPIR To maintain consistency in the noise level across our experiments, we employed the official code of DiffPIR (Zhu et al. [2023]) and adjusted the noise level parameter to 6.375.

PnP-ADMM We take the scico library’s implementation for our proposes. We set the ADMM penalty parameter $\rho = 0.2$ and maxiter = 12. Also, we leverage the pretrained DnCNN denoiser Zhang et al. [2017] for proximal

mapping.

ILVR For SR task, we followed ILVR and for other tasks we adopted projections onto convex sets (POCS) method, as in Chung et al. [2023], for inpainting Song et al. [2021] and Gaussian deblurring task.

C Ablation studies

C.1 Measurement Noise

We will demonstrate the robustness of our proposed method to varying noise levels. We will showcase the effectiveness of our approach under diverse noise conditions, highlighting its resilience against noise interference. DiffPIR’s reliance on a closed-form solution for conditional guiding grants it an advantage in noiseless scenarios. However, our method surpasses DiffPIR under varying noise levels, demonstrating its superior robustness.

Noise σ	0.0	0.025	0.05	0.1
DiffPIR	0.151	0.205	0.227	0.253
SaFaRI	0.154	0.193	0.212	0.242

Table 5: LPIPS comparison on measurement noise, FFHQ 256×256 -100 validation dataset, Gaussian deblurring task.

C.2 SR Scaling Factor

We evaluate our methods on the SR task using the LPIPS metric with various scaling factors. Table 6 demonstrates that the task becomes increasingly challenging as the scaling factor increases, which aligns with expectations.

Scaling Factor	×2	×4	×8	×16
LPIPS	0.116	0.191	0.270	0.247

Table 6: LPIPS evaluation of our method across various scaling factors of the SR task on FFHQ 256×256 -100 validation dataset.

C.3 Spatial Hyperparameters

Upsampling Factor To investigate the impact of varying upsampling factors r of the bicubic operator $\psi_{s,r}$ on the performance of our method, we evaluated the LPIPS metric across different scaling factors. The results, presented in Table 7, demonstrate a trend between the upsampling factor and LPIPS score.

Upsampling Factor	×2	×4	×8	×16
LPIPS	0.193	0.193	0.194	0.195

Table 7: LPIPS evaluation of our method across various upsampling factors of spatial operator $\psi_{s,r}$ for Gaussian Deblurring task on FFHQ 256×256 -100 validation dataset.

C.4 Frequency Hyperparameters

Radius r_0 In order to analyze the frequency context of the predicted measurement, the frequency domain is segmented into high-frequency and low-frequency components. The Fast Fourier Transform (FFT) algorithm is employed to transform the measurement data into the frequency domain. By applying an appropriate frequency shift, the low-frequency components are centered in the transformed image, facilitating the separation of the frequency domain into two distinct regions as illustrated in (13) and (14).

Parameter r_0 plays a pivotal role in governing the emphasis placed on specific frequency components. Consequently, the selection of an appropriate radius parameter r_0 is crucial for highlighting the desired fine-grained features. Table 8 demonstrates the impact of varying the r_0 .

Emphasizing parameters ρ_t^H, ρ_t^L Beyond the influence of r_0 , ρ_t^H and ρ_t^L also plays a significant role in determining the relative emphasis placed on high-frequency contextual information compared to low-frequency contextual information.

Table 9, 10 illustrate the effect of altering the relative proportions of high-frequency and low-frequency components. Insufficient values of ρ_t^H do not guarantee the generation of detailed images (Fig 4). Additionally, excessive values of ρ_t^L results in distorted and corrupted generated images (Fig 5).

r_0	1	2	3	4	5
SaFaRI	0.200	0.199	0.196	0.195	0.193

Table 8: LPIPS evaluation on radius r_0 of the Gaussian Deblurring task on FFHQ 256×256 -100 validation dataset.

$\rho_t^H \cdot 4\sqrt{\mathcal{L}_H}$	1	2	3	4	5
SaFaRI	0.220	0.207	0.201	0.196	0.193

Table 9: LPIPS evaluation on ρ_t^H , FFHQ 256×256 -100 validation dataset, Gaussian deblurring task with fixed ρ_t^L . The case $\rho_t^H \cdot 4\sqrt{\mathcal{L}_H} = 5$ represents the optimal case.

$\rho_t^L \cdot 4\sqrt{\mathcal{L}_L}$	1	2	3	4	5
SaFaRI	0.193	0.196	0.206	0.222	0.236

Table 10: LPIPS evaluation on ρ_t^L , FFHQ 256×256 -100 validation dataset, Gaussian deblurring task with fixed ρ_t^H . The case $\rho_t^L \cdot 4\sqrt{\mathcal{L}_L} = 1$ represents the optimized case.

D Further Experiments

We conduct additional quantitative analyses employing the standard metrics, PSNR and SSIM in Table 11 and Table 12. Also we present the further experimental results: from Figure 6 to Figure 13. Our method exhibits robust performance across a variety of tasks and datasets, as evidenced by comprehensive empirical evaluations.



Figure 4: The results of SaFaRI, Gaussian blurring under different ρ_t^H configurations. (left) The case $\rho_t^H = 0.25/\sqrt{\mathcal{L}_H}$ (middle) The case $\rho_t^H = 1.25/\sqrt{\mathcal{L}_H}$ (right) Ground Truth.

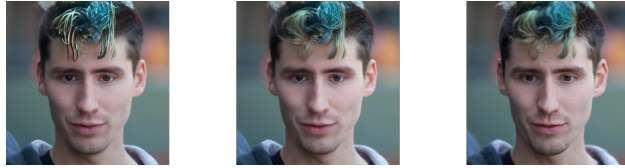


Figure 5: The results of SaFaRI, Gaussian blurring under different ρ_t^H configurations. (left) The case $\rho_t^L = 1.25/\sqrt{\mathcal{L}_L}$ (middle) The case $\rho_t^L = 0.25/\sqrt{\mathcal{L}_L}$ (right) Ground Truth.

Method	Inpaint (random)		Inpaint (box)		Deblur (Gauss)		SR ($\times 4$)	
	PSNR \uparrow	SSIM \uparrow	PSNR \uparrow	SSIM \uparrow	PSNR \uparrow	SSIM \uparrow	PSNR \uparrow	SSIM \uparrow
DPS Chung et al. [2023]	28.699	0.875	18.472	0.667	21.134	0.532	21.898	0.601
DiffPIR Zhu et al. [2023]	28.504	0.862	18.638	0.706	23.453	0.618	23.815	0.660
PnP-ADMM Chan et al. [2016]	18.467	0.584	13.310	0.579	21.788	0.595	23.444	0.702
ILVR Choi et al. [2021]	23.402	0.605	16.868	0.615	21.290	0.579	23.355	0.627
SaFaRI (ours)	28.732	0.880	18.887	0.778	23.064	0.642	23.703	0.680
SaFaRI-spatial (ours)	<u>28.753</u>	<u>0.880</u>	18.560	0.771	<u>23.098</u>	0.643	23.646	0.672
SaFaRI-freq. (ours)	28.833	0.881	<u>18.855</u>	0.779	22.862	0.629	<u>23.732</u>	<u>0.680</u>

Table 11: Quantitative evaluation of image restoration task with Gaussian noise ($\sigma = 0.025$) on ImageNet 256×256 -1k validation dataset. We compare our method with other zero-shot IR methods. We compute the metrics PSNR and SSIM for various tasks. **Bold**: Best, under: second best. (The ranking was done before the rounding)

Method	Inpaint (random)		Inpaint (box)		Deblur (Gauss)		SR ($\times 4$)	
	PSNR \uparrow	SSIM \uparrow	PSNR \uparrow	SSIM \uparrow	PSNR \uparrow	SSIM \uparrow	PSNR \uparrow	SSIM \uparrow
DPS Chung et al. [2023]	32.370	<u>0.933</u>	21.495	0.834	26.365	0.776	<u>27.539</u>	0.812
DiffPIR Zhu et al. [2023]	31.345	0.912	21.928	0.783	27.420	0.796	27.120	0.778
PnP-ADMM Chan et al. [2016]	18.634	0.605	12.587	0.560	24.746	0.759	26.412	0.834
ILVR Choi et al. [2021]	25.504	0.768	19.986	0.677	24.672	0.754	27.287	0.769
SaFaRI (ours)	32.534	0.933	23.492	0.852	<u>26.725</u>	<u>0.786</u>	27.538	0.812
SaFaRI-spatial (ours)	32.317	0.922	22.976	0.847	26.558	0.781	27.412	0.807
SaFaRI-freq. (ours)	<u>32.496</u>	0.934	<u>23.247</u>	<u>0.848</u>	26.709	0.786	27.556	<u>0.813</u>

Table 12: Quantitative evaluation of image restoration task with Gaussian noise ($\sigma = 0.025$) on FFHQ 256×256 -1k validation dataset. We compare our method with other zero-shot IR methods. We compute the metrics PSNR and SSIM for various tasks. **Bold**: Best, under: second best. (The ranking was done before the rounding)

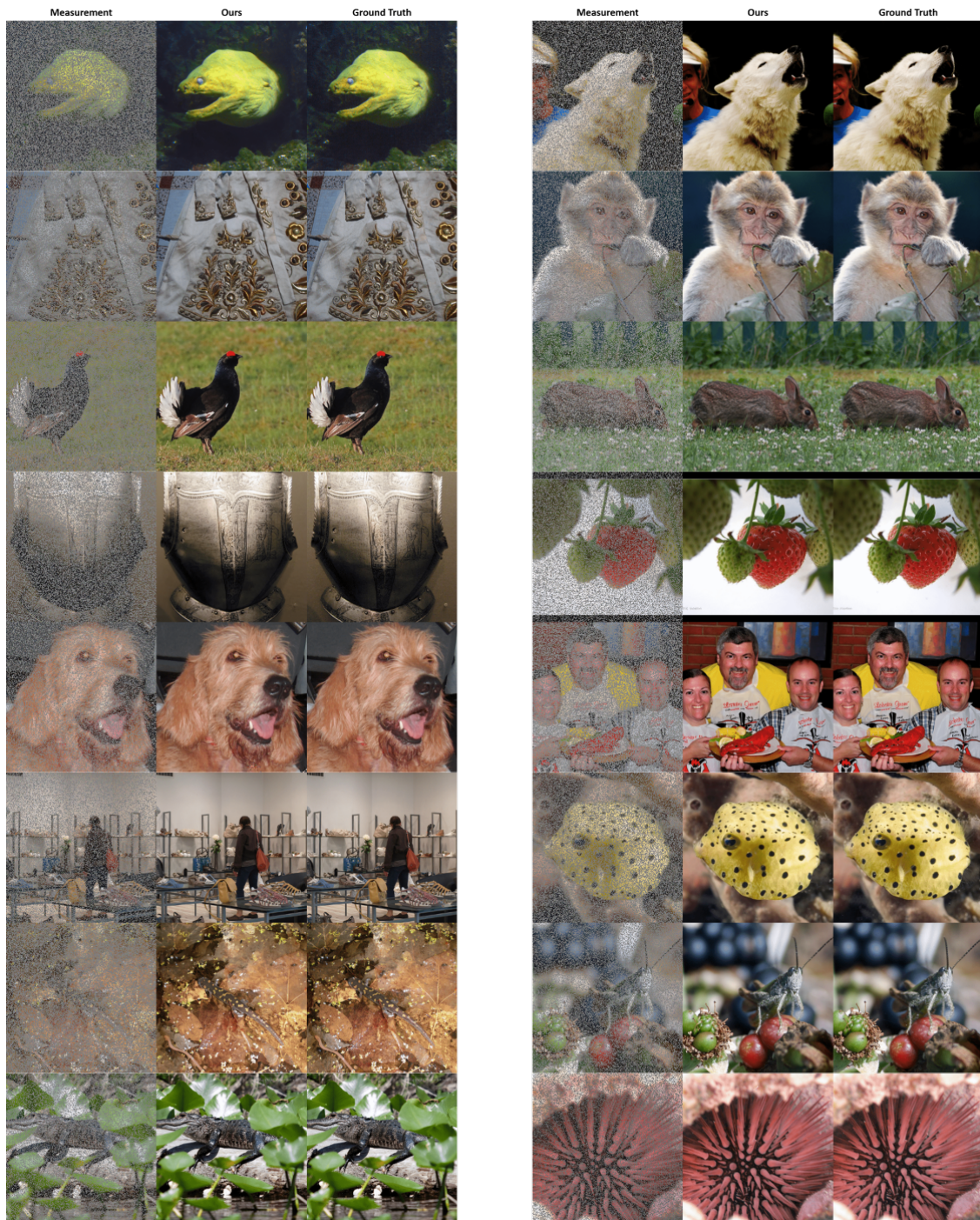


Figure 6: The results of SaFaRI, random-mask inpainting on the ImageNet 256×256 dataset.

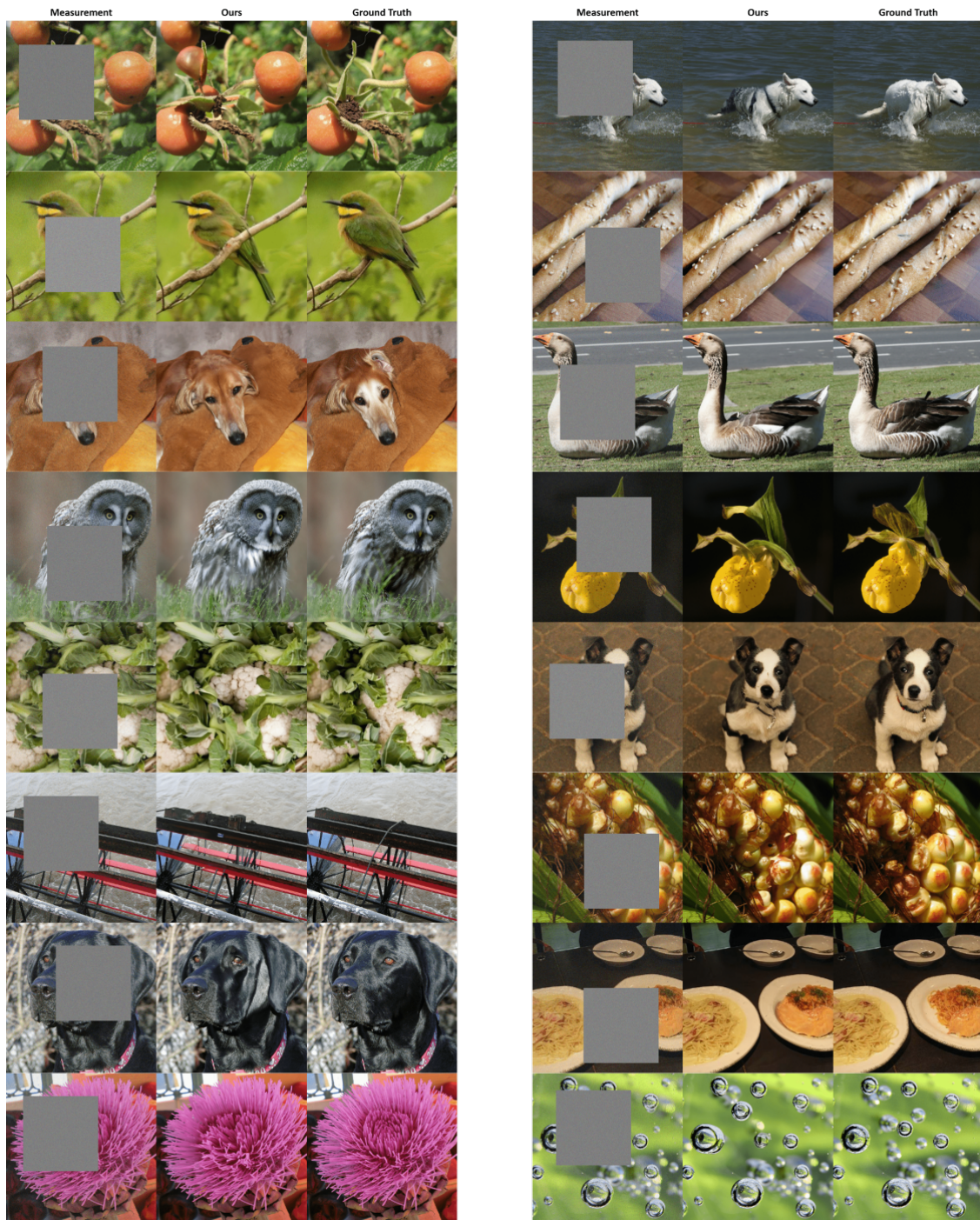


Figure 7: The results of SaFaRI, box-mask inpainting on the ImageNet 256×256 dataset.

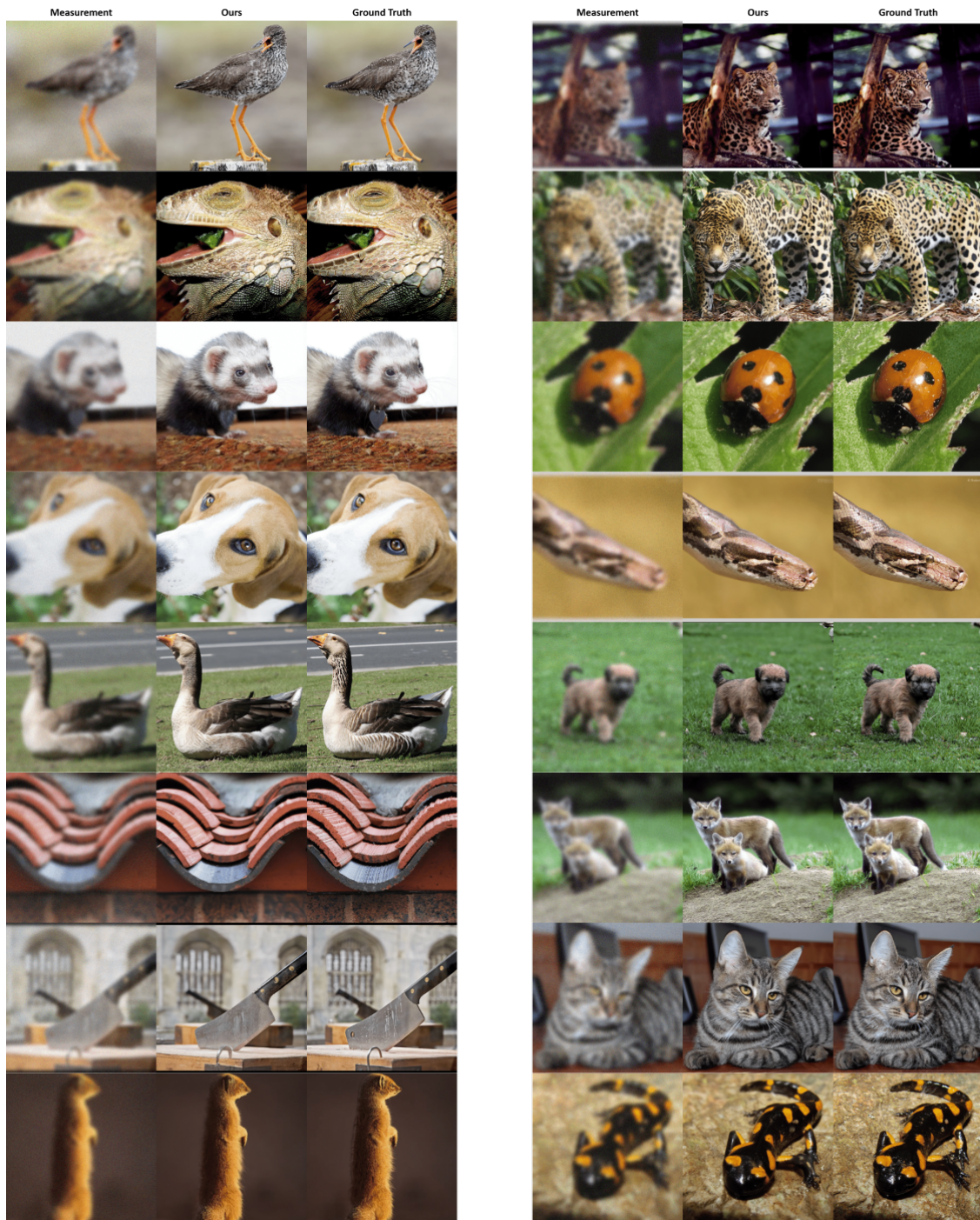


Figure 8: The results of SaFaRI, Gaussian deblurring on the ImageNet 256×256 dataset.

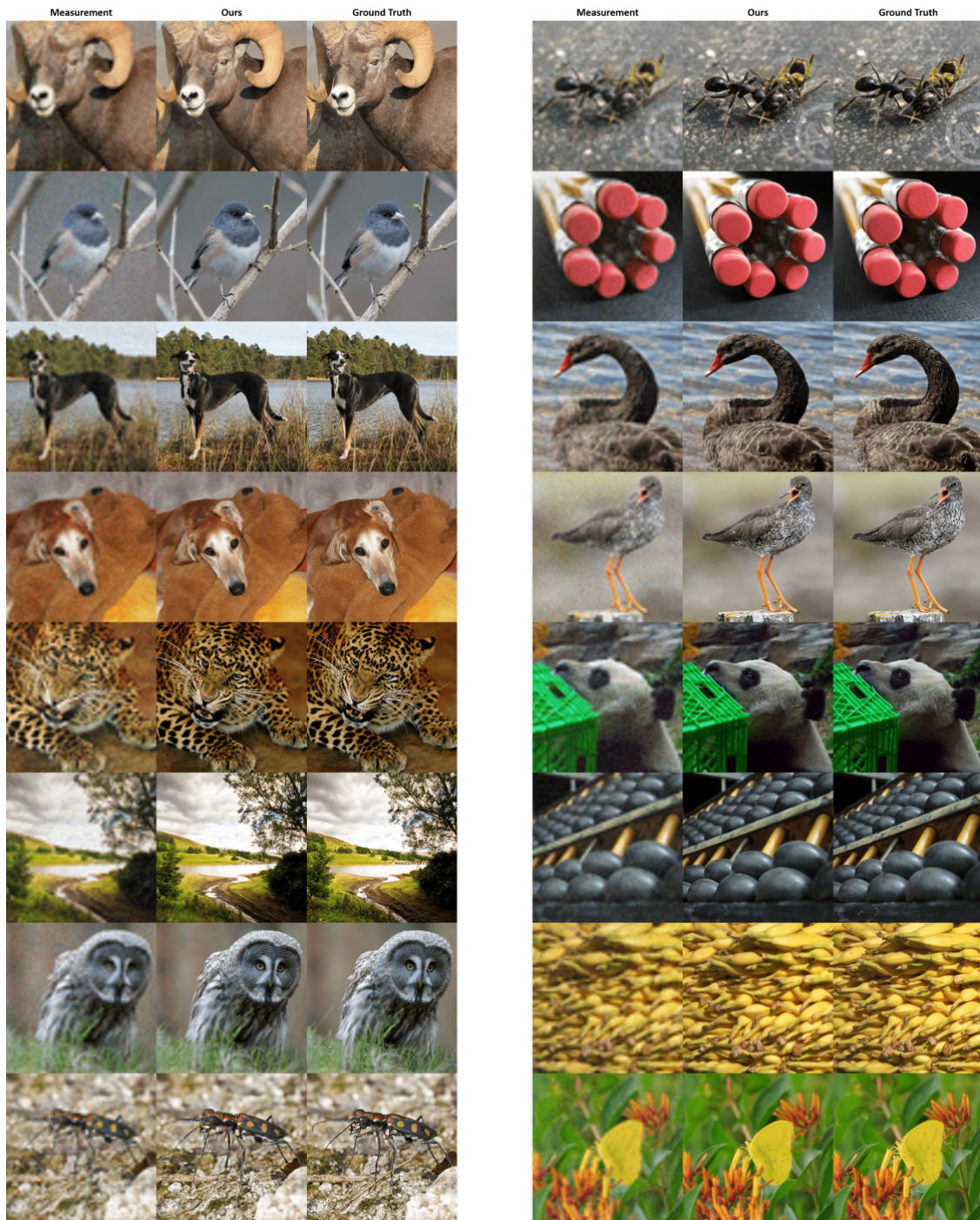


Figure 9: The results of SaFaRI, SR on the ImageNet 256×256 dataset.

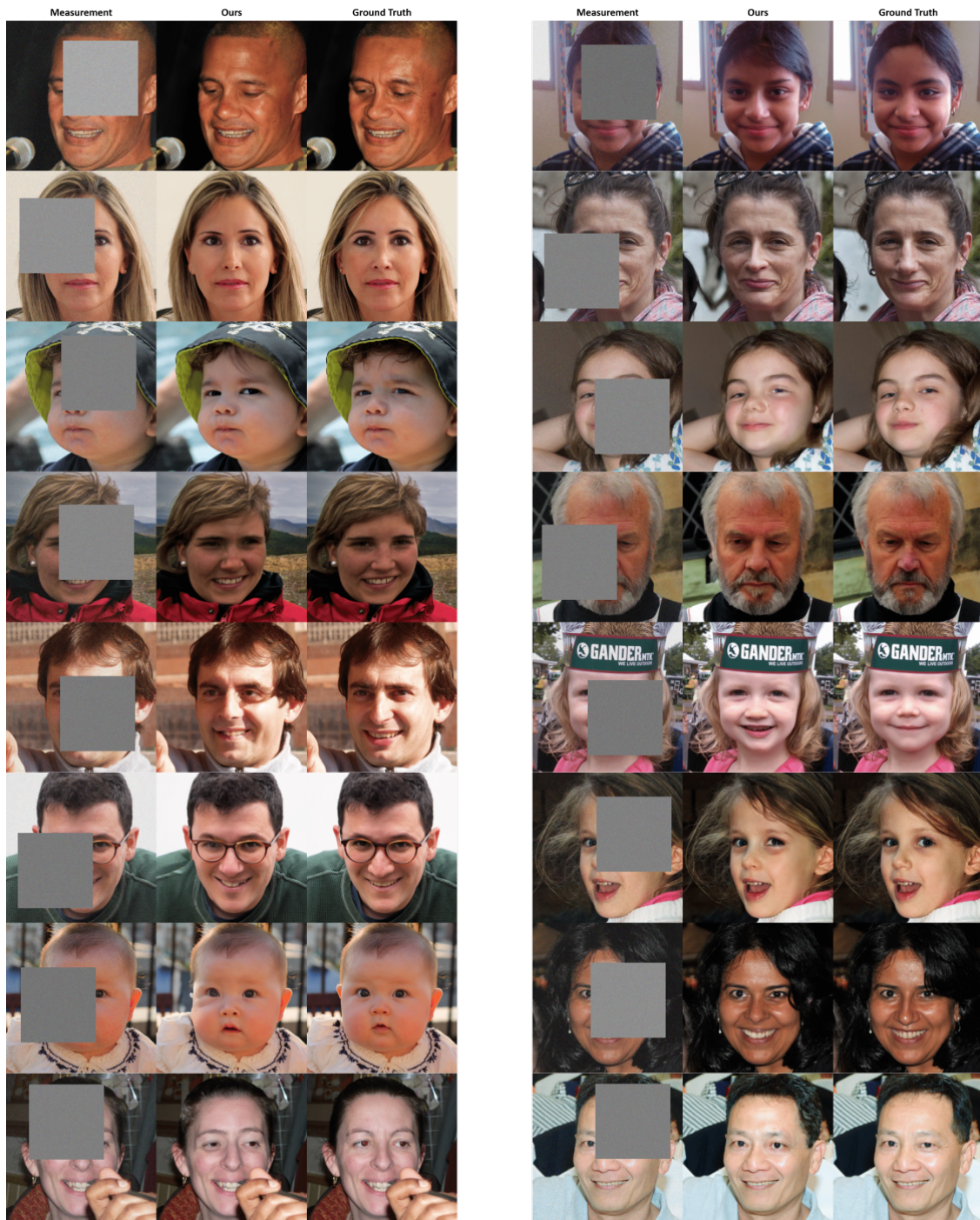


Figure 11: The results of SaFaRI, box-mask inpainting on the FFHQ 256×256 dataset.

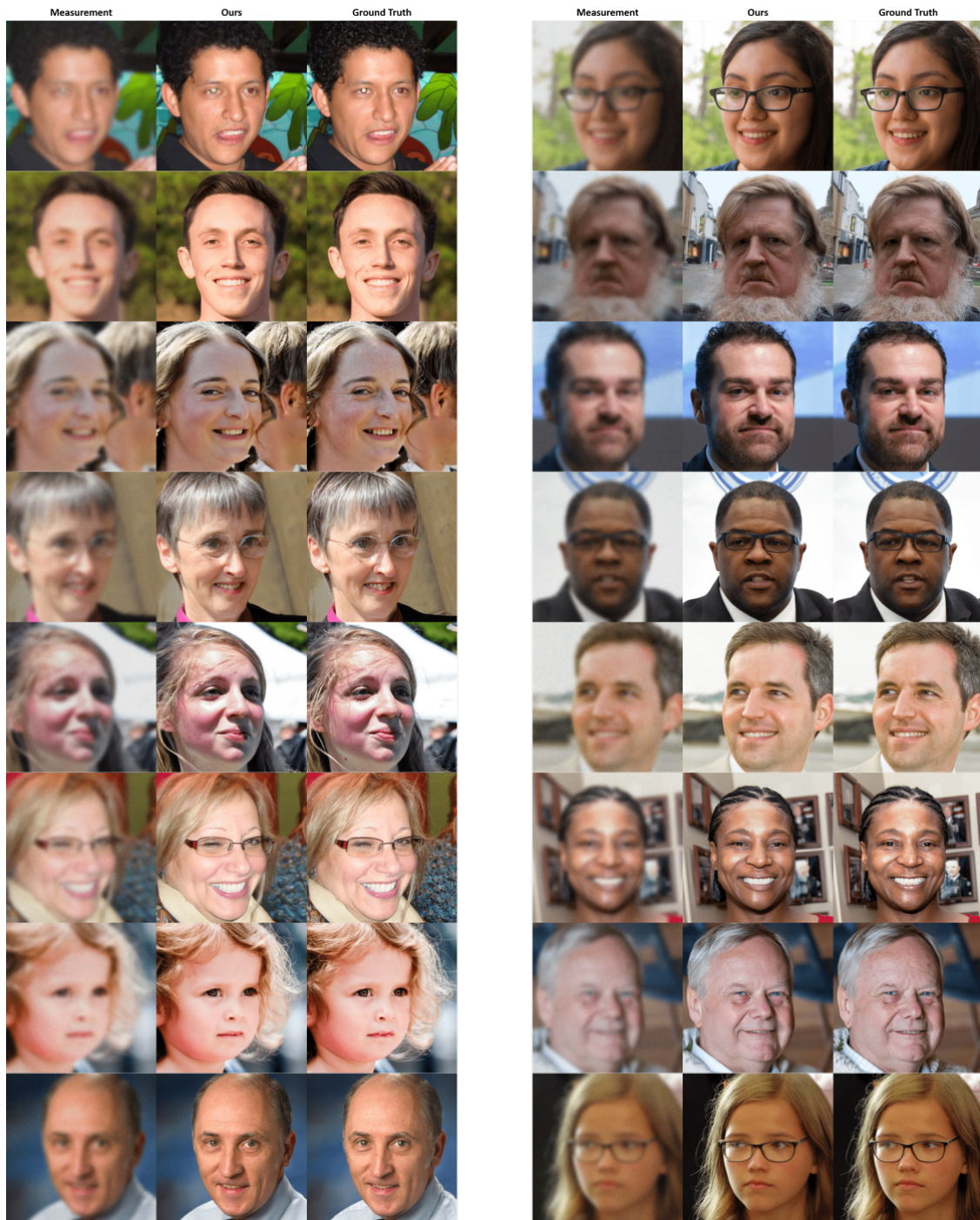


Figure 12: The results of SaFaRI, Gaussian deblurring on the FFHQ 256×256 dataset.

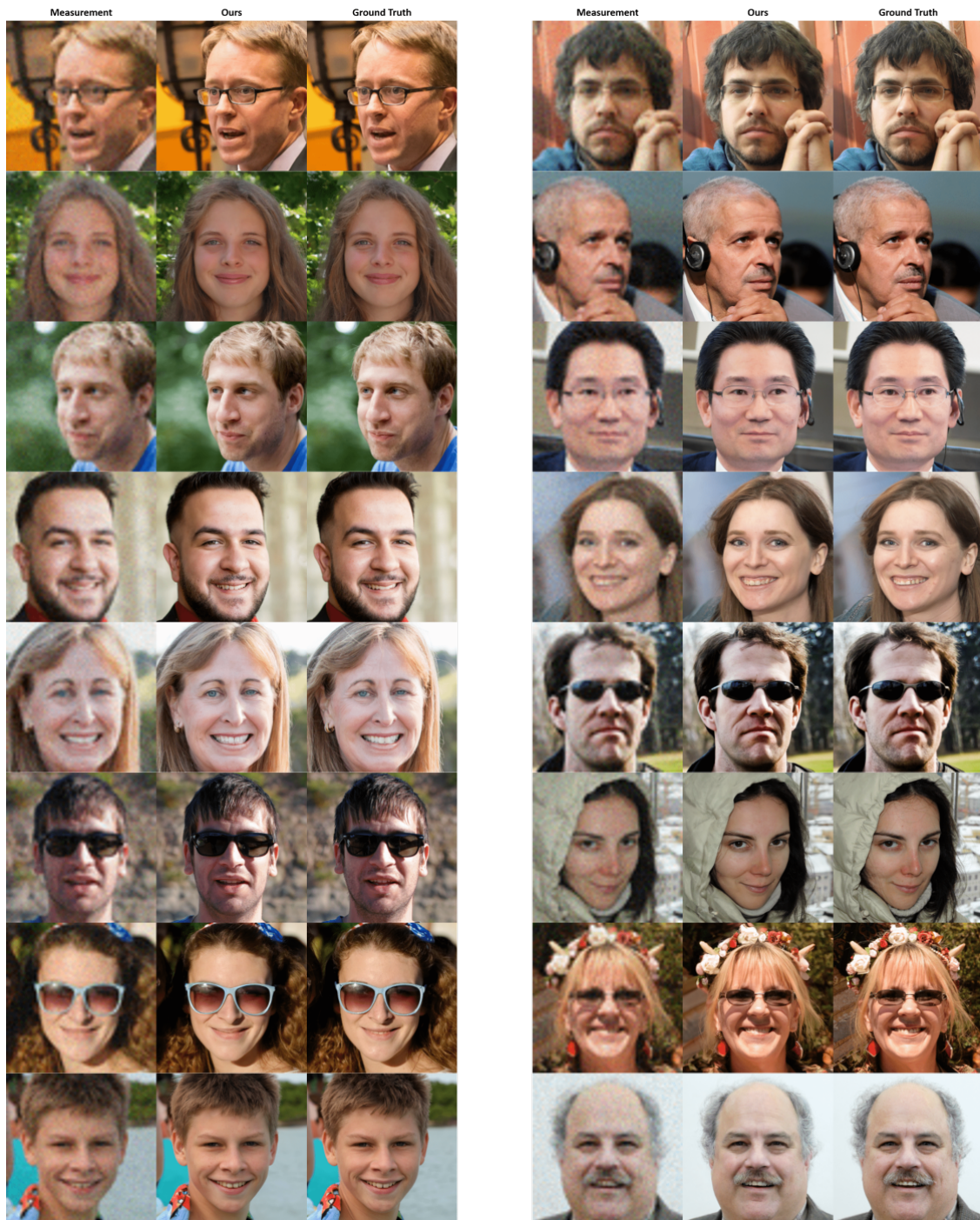


Figure 13: The results of SaFaRI, SR on the FFHQ 256×256 dataset.